Absorption of Short Laser Pulses on Solid Targets in the Ultrarelativistic Regime

Y. Ping,[1] R. Shepherd,[1] B. F. Lasinski,[1] M. Tabak,[1] H. Chen,[1] H. K. Chung,[1] K. B. Fournier,[1] S. B. Hansen,[1] A. Kemp,[1] D. A. Liedahl,[1] K. Widmann,[1] S. C. Wilks,[1] W. Rozmus,[2] and M. Sherlock[3]

[1]*Lawrence Livermore National Laboratory, Livermore, California 94550, USA*

[2]*Department of Physics, University of Alberta, Edmonton, Alberta, Canada, T6G 2G7*

[3]*Rutherford Appleton Laboratory, Chilton, United Kingdom*

(Received 6 April 2007; revised manuscript received 21 August 2007; published 28 February 2008)

We report the first direct measurements of total absorption of short laser pulses on solid targets in the ultrarelativistic regime. The data show an enhanced absorption at intensities above 10^{20} W/cm^2, reaching 60% for near-normal incidence and 80%–90% for 45° incidence. Two-dimensional particle-in-cell simulations demonstrate that such high absorption is consistent with both interaction with preplasma and hole boring by the intense laser pulse. A large redshift in the second harmonic indicates a surface recession velocity of 0.035c.

DOI: 10.1103/PhysRevLett.100.085004 PACS numbers: 52.25.Os, 52.38.Dx, 52.38.Kd, 52.65.Rr

The latest generation of advanced lasers delivers powerful laser pulses at petawatt (10^{15} W) levels [1], which, when focused, can reach intensities above 10^{20} W/cm^2. Such ultraintense laser pulses have been widely used in high-energy-density research [2–6]. However, relatively little experimental work has been dedicated to understand the details of laser absorption and subsequent energy partition among different pathways. There are studies on absorption at intensities up to 10^{18} W/cm^2 [7–9]. Recent experiments show that at 10^{20} W/cm^2, 10%–50% of laser energy is converted into hot electrons as inferred from x-ray dosimetry or $K\alpha$ yields [10–13].

In this Letter we report the first *direct* measurement of short laser pulse absorption at intensities 10^{17}–10^{20} W/cm^2. It is found that the absorption increases substantially in the ultrarelativistic regime. Our two-dimensional particle-in-cell (2D PIC) simulations with different conditions indicate that both preplasma and hole boring contribute to the large absorption.

The experiment was performed on the Callisto laser in the Jupiter laser facility (JLF) at Lawrence Livermore National Laboratory (LLNL). Callisto is a Ti:sapphire laser system delivering 150 fs laser pulses at 800 nm with energies up to 20 J. The intensity contrast of the 3 ns ASE pedestal to the main pulse is $\sim 10^{-8}$. The p-polarized laser pulse was focused by an $f/3$ off-axis parabola onto the target. The focal spot contained 50% of the energy within 5 μm full width at half maximum (FWHM), resulting in a maximum intensity of 3×10^{20} W/cm^2. The targets were Al foils with thickness 1.5–100 μm and 400 μm-thick Si plates. Our measurements did not show significant dependence of absorption on these target thickness and materials. Therefore, the data from the various targets are not distinguished in the results.

A custom-designed 30cm-diameter integrating sphere calibrated at the laser wavelength of 800 nm was employed to collect the scattered laser light (E_{scatter})—the same technique used in previous lower-intensity study [7–9]. The inner wall of the sphere was coated by a Lambertian scattering material, which has a reflectance $\geq 98\%$ over the spectral range of 300–2000 nm. We chose to measure the absorption at 6° (near-normal incidence) and 45°. The former is the closest case to S polarization, and the latter is representative of oblique incidence.

In the first experiment [Exp. 1 in Fig. 1(b)], E_{scatter} was measured by the sphere photodiode covered by an 800-nm interference filter with a bandwidth of 20 nm. In the second experiment [Exp. 2 in Fig. 1(b)], a visible spectrometer (200–1100 nm) was mounted onto the sphere and energy-calibrated at 800 nm to measure E_{scatter}. This visible spectrometer and another near-infrared spectrometer (700–2200 nm) were also used to measure the space-integrated energy fraction in harmonics (2ω, $3/2\omega$ and $1/2\omega$). The sphere had open ports for laser incidence and target alignment. The energy components not captured by the sphere, including backscattered energy (E_{back}, collected by a 2%

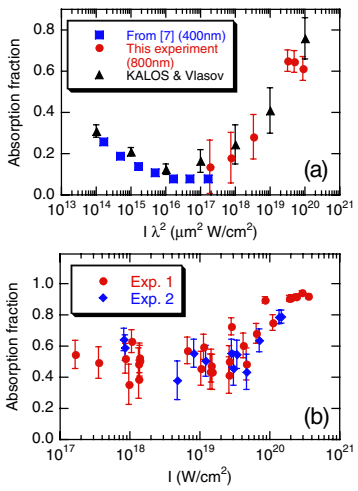

FIG. 1 (color online). Absorption fraction of the laser energy as a function of laser intensity at an incident angle of 6° (a) and 45° (b). Each point represents the result of a single laser shot.

beam splitter), reflected energy (E_{reflect}), and transmitted energy (E_{trans}), were measured by calibrated pyroelectric calorimeters. The total input energy (E_{in}) was determined by measuring a leak pulse that was cross-calibrated with the main pulse. The energy deposited in the target was then calculated as $E_{\text{abs}} = E_{\text{in}} - E_{\text{back}} - E_{\text{reflect}} - E_{\text{trans}} - E_{\text{scatter}}$ (the energy fraction in harmonics was found to be negligible). The absorption fraction is simply $E_{\text{abs}}/E_{\text{in}}$. Since the absorption is usually dependent on the scale length of the preplasma, a side-on interferometer (SOI) with a 100 fs, 400 nm probe pulse was set up to monitor the preplasma density profile. The probe was timed 10 ps before the main pulse and the spatial resolution was ~ 3 μm.

The measured energy absorption as a function of laser intensity at 6° and 45° is plotted in Figs. 1(a) and 1(b), respectively. The intensity was varied simply by changing the laser energy without moving the target. Previously published data [7] for normal incidence at low intensities are also plotted in Fig. 1(a) for comparison. Because the previous measurements were preformed at a different laser wavelength ($\lambda = 400$ nm), the horizontal coordinate of Fig. 1(a) is $I\lambda^2$. Our measurements are consistent with previously published data at low intensities ($I \sim 10^{17}$ W/cm^2), corroborating the validity of our measuring method. The results of this and previous experiments show a transition from collision-dominated absorption at $I\lambda^2 < 10^{17}$ W/cm^2 to collisionless absorption by collective processes [14], resulting in fast electron generation, at higher laser intensities. As the intensity increases, the absorption rises up to more than 60% at $I\lambda^2 \sim 10^{20}$ W/cm^2. We have used a 1D3V version of the Vlasov-Fokker-Planck code, KALOS [15], to model the laser-plasma interaction at near-normal incidence for 10^{15}–10^{19} W/cm^2. In the higher-intensity collisionless regime, $I\lambda^2 \sim 10^{19}$–10^{20} W/cm^2, the absorption was calculated with a 1D2V Vlasov code. A good agreement is obtained over the entire intensity range, as shown in Fig. 1(a). The error bars on the numerical results represent the upper and lower levels of absorption obtained in different runs with long ($L > \lambda$) and short ($L < \lambda$) scale lengths, respectively. At low intensities, $I\lambda^2 < 10^{17}$ W/cm^2, absorption is dominated by inverse bremsstrahlung [7] (a collisional process) which decreases for long scale lengths, while at higher intensities, $J \times B$ heating [16] (a collisionless process) dominates for normal incidence, which increases for long scale lengths.

For the 45° incidence, two sets of data were taken with slightly different methods (Exp. 1 and Exp. 2, as explained above). As shown in Fig. 1(b), they are in good agreement with each other. The absorption hovers around 50% from 10^{17} to $\sim 10^{19}$ W/cm^2, and then increases with the intensity, reaching a surprisingly high value (80%–90%) at $I \geq 10^{20}$ W/cm^2. The error bars are based on standard deviations in instrumental calibration. The error bar becomes smaller at higher absorption because what we measured was the "unabsorbed light", which was reduced relative to the total input due to high absorption. The scale length of the preplasma measured by SOI, defined as $L \equiv [\partial \ln(n_e)/\partial z]^{-1}$ where n_e is the plasma electron density, varies in a range of 3–15 μm. It was found that the maximum measurable density by this optical SOI is about 10^{20} cm^{-3}, which is only one tenth of the critical density (n_c).

To find out what processes contribute to the large absorption at oblique incidence, we performed 2D collisionless PIC simulations using Z3 [17] to interpret the measurements. In simulations, the conditions can be varied in a controlled manner to single out each process. First, we studied the effect of hole boring [18] on the absorption by using mobile ions or fixed ions in the code. Second, we chose three density profiles to elucidate the preplasma effect: no preplasma, "small preplasma" and "large preplasma" [19]. As shown in Fig. 2, the latter two have a density tail in agreement with a density profile measured by SOI that has a typical scale length $L \sim 6$ μm. In the case of small preplasma, the upper end of the underdense density slope is terminated at $0.2n_c$, while the large preplasma consists of an underdense density gradient up to $1.0n_c$. The low end of preplasma density was truncated at $0.088n_c$. The target density was set at $30n_c$ and the incident angle was 30° due to computational limitations. Two PIC runs at normal incidence show that the absorption at 3×10^{20} W/cm^2 is 72% with large preplasma and 60% with no preplasma, which is sufficiently different from the values at 30° incidence. Therefore, we think this angle is large enough to distinguish oblique incidence from normal incidence. The temporal pulse shape was a Gaussian with 150 fs FWHM.

The absorption fractions, calculated by substracting unabsorbed light from the total input energy in these 2D PIC simulations, are listed in Table I. Because the measurements show an enhancement of absorption from 10^{19} to 10^{20} W/cm^2, the simulations were carried out at two intensities: 1×10^{19} W/cm^2 and 3×10^{20} W/cm^2. When there is no preplasma and the ions are fixed, the absorption is only 37% at 3×10^{20} W/cm^2. If we let the ions move, hole boring can occur and the absorption rises up to 68%. When a small preplasma is added, the absorption shows a mild increase to 75%, while with a large preplasma the absorption is as high as 88%, very close to the measured value at this intensity. It is clear that the preplasma above

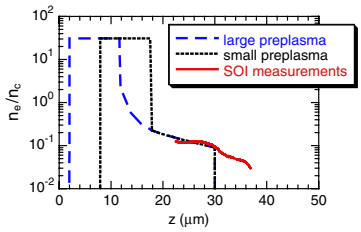

FIG. 2 (color online). Plasma density setup in 2D PIC simulations. The density profiles include large preplasma, small preplasma, and a measurement by SOI.

TABLE I. Absorption calculated by 2D PIC simulations.

Intensity (W/cm^2)	Ions	Preplasma	Absorption
3×10^{20}	Fixed	None	37%
3×10^{20}	Mobile	None	68%
3×10^{20}	Mobile	Small	75%
3×10^{20}	Mobile	Large	88%
3×10^{20}	Fixed	Large	63%
1×10^{19}	Fixed	None	25%
1×10^{19}	Mobile	None	35%
1×10^{19}	Mobile	Small	70%
1×10^{19}	Mobile	Large	85%

$0.2n_c$, which cannot be measured by the optical probe, plays an important role in absorption. This result points to the importance of developing x-ray interferometry or other techniques for more accurate scale length diagnostics. To verify that the high absorption is not solely due to the large preplasma, a simulation with fixed ions and large preplasma was performed, showing that the absorption drops to 63%. According to the simulation, among the 80%–90% total absorption, ~60% of the laser energy goes into kinetic energy of electrons, which is consistent with the conversion efficiency inferred from x-ray dosimetry [10]. The rest of the absorbed laser energy goes into kinetic energy of ion beams, hydrodynamic expansion and generation of strong fields inside the target, etc. For the case of 1×10^{19} W/cm^2, the absorption is 25% with fixed ions and no preplasma, which increases to 35% with mobile ions. The effect of hole boring is less significant than in the 3×10^{20} W/cm^2 case simply because of the less intense laser pulse. The 35% absorption with no preplasma and 70% with small preplasma are approximately the lower and upper limits of the measurements. If the large preplasma is present, the absorption can reach 85% even at 1×10^{19} W/cm^2.

A signature of hole boring is a redshift in the wavelength due to the Doppler effect from an inward-moving surface. This redshift has been observed at intensities up to 10^{19} W/cm^2 [20]. In our experiment, we chose the second harmonic for the redshift study because it originates from the relativistic critical surface. The spectrum was collected by a $f/10$ lens located in the specular direction for 45° incidence. The spectrum at 2×10^{20} W/cm^2 is redshifted by ~10 nm relative to that at 10^{18} W/cm^2. The surface velocity vs intensity is plotted in Fig. 3, showing a takeoff as the intensity rises above 10^{20} W/cm^2. Based on a simple model [18], the velocity of surface recession u_0 can be expressed as: $\frac{u_0}{c} = (\frac{1}{\gamma}\frac{Zm_e}{M_i}\frac{I\lambda^2}{2.74\times10^{18}})^{1/2}$, where γ is the relativistic factor. Taking into account the absorption and the oblique incidence, the final surface velocity is: $\frac{u}{c} = (\frac{2-f_{abs}}{2}\cos\theta)^{1/2}\frac{u_0}{c}$. Both calculation results with and without absorption are included in Fig. 3. The measured values of absorption were used, i.e. ~50% for 10^{18}–10^{19} W/cm^2, and ~90% for $I > 10^{20}$ W/cm^2. It is clear that at $I > 10^{20}$ W/cm^2, a good agreement is obtained when the absorption is taken into account, thus confirming the high absorption we observed. The model is less satisfactory at lower intensities because it does not include the effect of plasma thermal pressure, which may balance or even exceed the ponderomotive force when the laser pulse is less intense. The surface velocity reaches 10 nm/fs at $I > 10^{20}$ W/cm^2. As a result, the hole boring can play an important role even for 100 fs pulses in the ultrarelativistic regime.

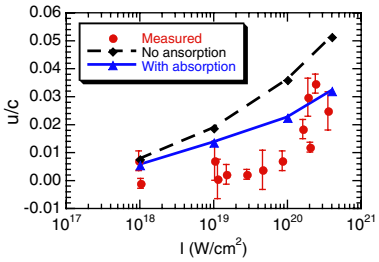

FIG. 3 (color online). Comparison of the surface velocity calculated from the Doppler redshift of specular-reflected 2ω to a simple model with and without absorption.

To further understand the underlying absorption mechanisms, we proceeded to measure the angular distribution of hot electrons. It is known that at oblique incidence the existence of plasma in front of the target gives rise to resonance absorption [21], generating hot electrons preferentially normal to the target surface. At high intensities, $J \times B$ heating [16] can occur, which pushes electrons in the laser direction. Therefore, the spatial features of hot electrons provide a signature of the dominant absorption mechanism. To measure this, the integrating sphere was replaced by a 30-cm-diameter dosimeter holder located in the laser incident plane with the target at the center. Thermoluminescence dosimeters (TLD) were mounted on the holder to measure the angular distribution of hot electrons. The TLDs were covered by aluminum filters to block low-energy electrons and almost all ions. The thickness of the Al filters was varied according to the laser intensity so that the most energetic electrons were measured. The ultrathin thickness of TLD ensures that the hot electron contribution is dominant over the x-ray contribution to the dose [22]. This has been confirmed by simultaneous measurements by TLD and a calibrated electron spectrometer in another experiment.

The angular distributions of hot electrons measured by TLD with a resolution of 10° at three intensities for 45° incidence are shown in Fig. 4. The thickness of the Al filters for the TLDs was varied from 100 μm to 500 μm, and to 2mm for these three intensities, blocking electrons with energies below 100 keV, 350 keV, and 1 MeV, respectively. We observed progressive enhancement of hot electrons at the back side of target with increasing the laser intensity. At a low intensity of 8×10^{17} W/cm^2 [Fig. 4(a)], most of the hot electrons are emitted at the front side. As the intensity increases to 2×10^{19} W/cm^2

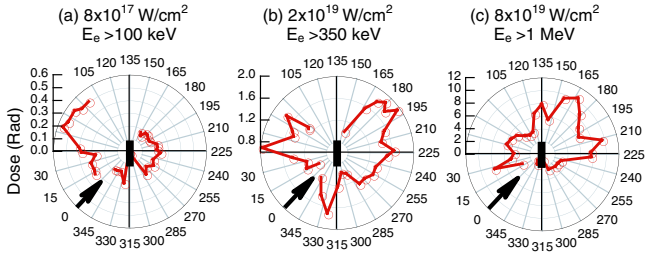

FIG. 4 (color online). Angular distributions of hot electrons measured by TLD at three intensities (laser direction and target orientation marked by the arrow and the line).

[Fig. 4(b)], the backside component increases to become comparable with the front side part, and there is a distinct peak in the laser direction, showing that the $J \times B$ heating starts to play a role. As the intensity reaches 8×10^{19} W/cm^2 [Fig. 4(c)], hot electrons at the backside are dominant, with peaks in the laser direction and target normal, which arise from resonance absorption and $J \times B$ heating, respectively. The relative amplitude of these two peaks varies from shot to shot, and they often combine into one broad peak. There is also a peak along the target surface, consistent with the surface jet observed at low intensities [23]. However, this feature is not very reproducible. The details of the angular distribution of hot electrons deserve further study and should be addressed in the future with higher angular resolution and better controlled experimental conditions. Laser-driven instabilities, such as two-plasmon decay and Raman scattering, may also take place and generate hot electrons. According to our half-harmonics measurements, which are a signature of these processes [24], the $1/2\omega$ and $3/2\omega$ are less than 12% of the unabsorbed 1ω, and hence, less than 1% of total laser energy with 90% absorption. Therefore, these underdense instabilities are present but may not be significantly energetic in the energy partition.

To summerize, we have measured the total absorption of short laser pulses at intensities of 10^{17}–10^{20} W/cm^2. It is found that the absorption is enhanced at $I \geq 10^{20}$ W/cm^2, reaching 60% for near-normal incidence and 80%–90% for 45° incidence. Our 2D PIC simulations with selective conditions demonstrate that preplasma and hole boring contribute to the enhanced absorption at oblique incidence. These results will lay the foundation for both basic and applied research involving ultraintense short laser pulses. One relevant application is the fast ignition. However, the driving pulse for fast ignition is much longer (~10 ps); hence, electron transport will play an important role. We plan to study the effect of transport on absorption in the near future.

We wish to thank the laser operation team of JLF at LLNL. We would also like to acknowledge A. B. Langdon and C. H. Still for helpful consultations on the Z3 simulations, and B. Berry and A. Niles for technical support. This work was performed under the auspices of U. S. DOE by LLNL under Contract No. W-7405-eng-48.

[1] M. D. Perry and G. Mourou, Science **264**, 917 (1994).
[2] B. A. Remington, D. Arnet, R. P. Drake, and H. Takabe, Science **284**, 1488 (1999).
[3] M. H. Key, Nature (London) **412**, 775 (2001); T. Ditmire *et al.*, Nature (London) **398**, 489 (1999).
[4] M. Tabak *et al.*, Phys. Plasmas **1**, 1626 (1994); R. Kodama *et al.*, Nature (London) **418**, 933 (2002).
[5] S. P. D. Mangles *et al.*, Nature (London) **431**, 535 (2004); C. G. R. Geddes *et al.*, Nature (London) **431**, 538 (2004); J. Faure *et al.*, Nature (London) **431**, 541 (2004).
[6] E. L. Clark *et al.*, Phys. Rev. Lett. **84**, 670 (2000); A. Maksimchuk *et al.*, *ibid.* **84**, 4108 (2000); R. A. Snavely *et al.*, *ibid.* **85**, 2945 (2000).
[7] D. F. Price *et al.*, Phys. Rev. Lett. **75**, 252 (1995).
[8] E. T. Gumbrell *et al.*, Phys. Plasmas **5**, 3714 (1998).
[9] M. Borghesi, A. J. Mackinnon, R. Gaillard, O. Willi, and D. Riley, Phys. Rev. E **60**, 7374 (1999).
[10] S. P. Hatchett *et al.*, Phys. Plasmas **7**, 2076 (2000).
[11] M. H. Key *et al.*, Phys. Plasmas **5**, 1966 (1998).
[12] W. Theobald *et al.*, Phys. Plasmas **13**, 043102 (2006).
[13] J. Myatt *et al.*, Phys. Plasmas **14**, 056301 (2007).
[14] S. C. Wilks and W. L. Kruer, IEEE J. Quantum Electron. **33**, 1954 (1997).
[15] A. R. Bell *et al.*, Plasma Phys. Controlled Fusion **48**, R37 (2006).
[16] W. L. Kruer and K. Estabrook, Phys. Fluids **28**, 430 (1985).
[17] Z3 is a modern massively-parallel 3D rewrite of the methods in C. K. Birdsall and A. B. Langdon, *Plasma Physcis via Computer Simulation* (McGraw-Hill, New York, 1985).
[18] S. C. Wilks, W. L. Kruer, M. Tabak, and A. B. Langdon, Phys. Rev. Lett. **69**, 1383 (1992).
[19] A hydrodynamic simulation using LASNEX with the laser contrast at 10^{20} W/cm^2 shows a higher electron density near the target surface, with a scale length of 2.9 μm at n_c, compared with 2.1 μm in the "large preplasma" profile. This may lead to higher absorption in PIC runs. However, since the absorption is already very high (~90%), using the LASNEX profile will not qualitatively change our interpretation of the absorption data.
[20] X. Liu and D. Umstadter, Phys. Rev. Lett. **69**, 1935 (1992); M. P. Kalashnikov *et al.*, *ibid.* **73**, 260 (1994); R. Kodama *et al.*, *ibid.* **77**, 4906 (1996); M. Zepf *et al.*, Phys. Plasmas **3**, 3242 (1996).
[21] See, for example, W. L. Kruer, *Physics of Laser Plasma Interactions* (Addison-Wesley, Menlo Park, CA, 1988).
[22] P. Bilski, P. Olko, B. Burgkhardt, and E. Piesch, Radiation Measurements **24**, 439 (1995).
[23] Y. T. Li *et al.*, Phys. Rev. Lett. **96**, 165003 (2006).
[24] D. A. Russell and D. F. DuBois, Phys. Rev. Lett. **86**, 428 (2001); L. Veisz *et al.*, Phys. Plasmas **11**, 3311 (2004).